Development of a Non-Local Neoclassical Transport Code for Helical Configurations

Shinsuke SATAKE[1)], Ryutaro KANNO[1,2)] and Hideo SUGAMA[1,2)]

[1)]*National Institute for Fusion Science, 322-6 Oroshi-cho, Toki 509-5292, Japan*
[2)]*Department of Fusion Science, Graduate University for Advanced Studies, Toki 509-5292, Japan*

The progress in a 3-dimensional, non-local neoclassical transport simulation code "FORTEC-3D" is described. The main purpose of the code is to solve the drift-kinetic equation in general a 3-dimensional configuration using the δf Monte Carlo method, and to calculate neoclassical fluxes and the time evolution of the ambipolar radial electric field simultaneously. This article explains new numerical schemes adopted in FORTEC-3D in order to overcome numerical problems, which happen especially in the cases where the bifurcation of radial electric field occurs. Examples of test simulation for an LHD magnetic field configuration with a bifurcated electric field are also shown. With improved numerical schemes, FORTEC-3D can calculate neoclassical fluxes and trace the time evolution stably for several ion collision times, which is sufficiently long to observe GAM damping and formation of the ambipolar electric field.

1. Introduction

Detailed calculation of neoclassical transport in 3-dimensional configuration plasmas such as Large Helical Device (LHD) is important for transport analysis, since in a 3-dimensional system, the ambipolar condition $\Gamma_i(\rho, E_\rho) = \Gamma_e(\rho, E_\rho)$ determines the radial electric field profile $E_\rho(\rho)$, where Γ_i and Γ_e are ion and electron particle fluxes across the flux-surface $\rho =$const. It is known that the ambipolar condition is determined mainly by neoclassical transport. If the ambipolar condition has multiple roots, bifurcation of radial electric field profile occurs [1]. In LHD plasmas, appearance of positive electric field, the "electron root," is preferable since it reduces neoclassical transport compared with that in negative one, the "ion root" [2]. Moreover, strongly sheared electric field profile at the transition layer is generally considered to be favorable from the viewpoint of suppression of anomalous transport.

Neoclassical transport theory for a 3-dimensional helical configuration [3,4] has been constructed under the assumption of local transport model, where the typical orbit width in the minor-radius direction is assumed to be negligible compared with the background gradient scale lengths of a plasma. Recently, non-local or finite-orbit-width (FOW) effects on neoclassical transport have attracted attention in the analysis of core transport in tokamaks. There appear potato particles with large orbit widths, and these particles violate the assumption of conventional neoclassical theory [5, 6]. In helical configurations, the deeply

ripple-trapped and transition particles drift long distance in radial directions. The FOW effect of these orbits will be important in neoclassical transport analysis, if the ion temperature at the core is high and the collisionality becomes very low, as in the high-T_i operation in LHD [7]. On the other hand, radial drift motion of particle is restricted in the presence of $\boldsymbol{E} \times \boldsymbol{B}$ rotation. Further the change in particle drift in turn affects the ambipolar condition. The presence of a strong-sheared electric field will also cause a non-local effect to neoclassical transport. Thus, it is important to solve both neoclassical transport and formation of ambipolar radial electric field self-consistently and simultaneously, with the FOW effects taken into consideration. However, the applicability of analytic neoclassical theory to this issue is questionable since it neglects the FOW effect from the beginning. It should also be pointed out that most of the conventional neoclassical transport theory and analytic formulae assume the quasi-stationary state. Thus, they are not applicable for tracing the rapid time evolution of radial electric field as fast as particle transit time $\tau_{tr} \sim qR/v_{th}$, similar to the case of the geodesic acoustic mode (GAM) [8].

From the considerations above, we have been developing a simulation code to solve the drift-kinetic equation (DKE) including the FOW effect in a 3-dimensional configuration. The simulation code, FORTEC-3D [9–11], uses the δf Monte Carlo method [12, 13], which has been applied in some other transport codes both for tokamaks [14] and for helical configurations [15, 16]. The features

of FORTEC-3D are as follows: (1) It uses a conserved-form linearized Fokker-Planck collision operator. (2) It is a global simulation code. The entire confinement region is solved at once. (3) Time evolution of the radial electric field is solved simultaneously. The ambipolar electric field is then determined in consistency with neoclassical fluxes. To reduce calculation time for practical use, only ion transport is solved by the δf method, and electron transport is solved by the GSRAKE code [17], which solves bounce-averaged DKE. Note that the GSRAKE solution does not include the FOW effect, and then only the non-local effect for ions transport is treated in FORTEC-3D.

So far FORTEC-3D has been applied successfully for LHD configurations to solve the formation of ambipolar field for ion roots [9], and to study the configuration dependence and the FOW effect of GAM oscillation and damping [10, 11]. However, from several test calculations, we found it difficult to apply FORTEC-3D to the cases with electron roots, since the bifurcated radial electric field profile attained an unphysical shape as shown later. We also found that the numerical noise in particle flux and the numerical error in collision operator were intolerably large, which had not been found in tokamak cases. We ascertained that these problems resulted from inaccuracy in the way of using radial grids to evaluate flux and electric field, and from the emergence of huge-weight markers caused by large radial drift from the initial position. Both points should be treated carefully in transport simulations where the non-local nature of neoclassical transport is important.

In this paper, improvements for numerical schemes in FORTEC-3D applied recently to overcome the problems above are explained. In section 2, basic equations for the δf Monte Carlo method are reviewed. In section 3, modification of collision operator is described. The new operator has good conservation property with less marker numbers. In section 4, improvement in the evaluation of flux and electric field are explained. Adoption of staggered mesh in radial direction to evaluate these two quantities enables simulation of the formation of bifurcated radial electric field profile stably. In section 5, new filtering scheme for marker weights to reduce numerical noise is introduced. By comparing several tests with varied strength of filters, it is shown that the filtering scheme does not affect the solutions. As a result of these improvements, FORTEC-3D is ready to solve neoclassical transport in helical plasmas in varied profiles and simulate evolution of electric fields including bifurcations.

2. Basic Equations of the δf Method

In the δf method, time development of the perturbation of guiding-center distribution function from the background local Maxwellian $\delta f = f - f_M$ is solved according to the following drift-kinetic equation [10]

$$\frac{\mathrm{D}}{\mathrm{D}t}\delta f(X, \mathcal{K}, \mu, t) \equiv \frac{\partial \delta f}{\partial t} + (v_\parallel + v_\mathrm{d}) \cdot \nabla \delta f$$

$$+ \dot{\mathcal{K}}\frac{\partial \delta f}{\partial \mathcal{K}} - C_\mathrm{tp}(\delta f)$$

$$= -\left(v_\mathrm{d} \cdot \nabla f_\mathrm{M} + \dot{\mathcal{K}}\frac{\partial f_\mathrm{M}}{\partial \mathcal{K}}\right) + \mathcal{P} f_\mathrm{M}, \tag{1}$$

where C_tp and $\mathcal{P}$ are the test-particle and field-particle parts of the linearized collision operator, respectively. Here, kinetic energy $\mathcal{K} = mv^2/2$ is chosen as an independent variable instead of the total energy $\mathcal{E} = \mathcal{K} + e\Phi$ to describe DKE, since we allow an electrostatic potential Φ that depends on time. The magnetic moment $\mu = mv_\perp/2B$ is a constant of motion, and the term $\dot{\mu}\partial/\partial\mu$ does not appear in Eq. (1). An MHD equilibrium magnetic field is constructed from the VMEC code [18], and it is sent to FORTEC-3D in the Boozer coordinate system (ψ, θ, ζ) [19] as $B = \nabla\psi \times \nabla\theta + \iota\nabla\zeta \times \nabla\psi$. In practice, we use ρ for a normalized radial coordinate defined from toroidal flux ψ as $\rho = \sqrt{\psi/\psi_\mathrm{out}}$. The background temperature, density, and electrostatic potential are considered as flux-surface functions, thus $f_\mathrm{M} = f_\mathrm{M}(\rho, \mathcal{K})$. The time evolution of radial electric field $E = -(\mathrm{d}\Phi/\mathrm{d}\rho)\nabla\rho = E_\rho\nabla\rho$ is solved from the following equations

$$\epsilon_0\epsilon_\perp \frac{\partial E_\rho}{\partial t} = -e\left[z_\mathrm{i}\Gamma_\mathrm{i} - \Gamma_\mathrm{e}\right], \tag{2a}$$

$$\Gamma_\mathrm{i,e} = \left\langle \int \mathrm{d}^3 v v_\mathrm{d} \cdot \nabla\rho\, \delta f_\mathrm{i,e} \right\rangle, \tag{2b}$$

where subscripts i and e describe particle species, $\langle\cdots\rangle$ indicates a flux-surface average, and the factor $\epsilon_\perp \equiv \left[\left\langle |\nabla\rho|^2\right\rangle + \left\langle c^2|\nabla\rho|^2\right\rangle /v_\mathrm{A}^2\right]$ represents the permittivity, which includes the classical polarization drift effect.

To solve Eq. (1), two weights for simulation markers, w and p, are introduced, which satisfy the relations $wg = \delta f$ and $pg = f_\mathrm{M}$, respectively, where g is 5-dimensional simulation marker distribution function. Since D/Dt indicates the derivative along the guiding-center motion in the phase space $(\rho, \theta, \zeta, \mathcal{K}, \mu)$ including the random-walk in velocity space by C_tp operator, we have Dg/D$t = 0$. Then the time evolution of marker weights is given by

$$\frac{\mathrm{D}w}{\mathrm{D}t} = \frac{p}{f_\mathrm{M}}\left[-v_\mathrm{d} \cdot \nabla - \dot{\mathcal{K}}\frac{\partial}{\partial\mathcal{K}} + \mathcal{P}\right]f_\mathrm{M}, \tag{3a}$$

$$\frac{\mathrm{D}p}{\mathrm{D}t} = \frac{p}{f_\mathrm{M}}\left[v_\mathrm{d} \cdot \nabla + \dot{\mathcal{K}}\frac{\partial}{\partial\mathcal{K}}\right]f_\mathrm{M}. \tag{3b}$$

The numerical procedures for the collision operator and for Eqs. (2) are described in the following sections.

3. Collision Operator

The linearized Fokker-Planck operator in FORTEC-3D is made to satisfy the following relations [20],

$$\int \mathrm{d}^3 v \mathcal{M}\left(C_\mathrm{tp}(\delta f) + \mathcal{P} f_\mathrm{M}\right) = 0 \quad \text{for} \quad \mathcal{M} = \{1, v_\parallel, v^2\}, \tag{4}$$

$$C_\mathrm{tp}(\delta f) + \mathcal{P} f_\mathrm{M} = 0 \quad \text{for} \quad \delta f = (c_0 + c_1 \cdot v + c_2 v^2)f_\mathrm{M}. \tag{5}$$

The test-particle operator C_{tp} is expressed by random scattering of marker velocity in the $(v_{\parallel}, v_{\perp})$-space. The field-particle operator is given in following form

$$\mathcal{P} = -\frac{1}{n}\left[aF(x) + bG(x)\xi + cH(x)\right], \qquad (6\text{a})$$

$$F(x) = 1 - 3\sqrt{\frac{\pi}{2}}x^{-1/2}\left(\phi(x) - \frac{\text{d}\phi(x)}{\text{d}x}\right), \qquad (6\text{b})$$

$$G(x) = 3\sqrt{\frac{\pi}{2}}x^{-1}\phi(x), \qquad (6\text{c})$$

$$H(x) = 3\sqrt{\frac{\pi}{2}}x^{-1/2}\left(\phi(x) - \frac{\text{d}\phi(x)}{\text{d}x}\right), \qquad (6\text{d})$$

where $x \equiv v^2/v_{\text{th}}^2$, $\xi \equiv v_{\parallel}/v$, $\phi(x) = \left(2/\sqrt{\pi}\right)\int_0^x \text{d}t\exp^{-t}\sqrt{t}$ is the error function, and n and v_{th} are the density and temperature of background f_{M}, respectively. The factors (a, b, c) are determined so that the field-particle operator $\mathcal{P}f_{\text{M}}$ cancels the changes in constants of motions by C_{tp}, e.g.,

$$\{\delta n, \delta P, \delta E\} = \int \text{d}^3v\left\{1, v_{\parallel}, v^2\right\}C_{\text{tp}}(\delta f). \qquad (7)$$

In the ideal limit where the relations $wg = \delta f$ and $pg = f_{\text{M}}$ are strictly satisfied, these factors are determined as $(a, b, c) = (\delta n, 2\delta P/v_{\text{th}}, 2\delta E/(3v_{\text{th}}^2))$ using Eq. (4). Note that the test-particle operator itself never changes the number of particles. However, after a series of operations of test- and field-particle operators, there still remains numerical error in constants of motions, including δn. To reduce the error, in the previous FORTEC-3D code, the remaining errors after $(i-1)$ times operation of $\mathcal{P}f_{\text{M}}$

$$\{\delta n, \delta P, \delta E\}_i = \int \text{d}^3v\left\{1, v_{\parallel}, v^2\right\}\left[C_{\text{tp}}(\delta f) + \sum_{k=0}^{i-1}\mathcal{P}_k f_{\text{M}}\right]$$

are evaluated, and then i-th field-particle operation to marker weight $\text{d}w/\text{d}t = p \times \mathcal{P}_i$ is executed again [12]. This recursive procedure has worked well to reduce numerical error with 2- or 3- time recursive operations in previous tokamak simulation. However, it was found that the numerical error in the conservation law (4) becomes larger in 3-dimensional helical configuration cases. In helical cases, it is difficult to maintain sufficient marker population in a unit volume, and the marker distribution g is distorted in the velocity space in the presence of ripple-trapped particles, which result in deterioration in the expression of plasma distribution functions δf and f_{M} with finite markers. This also causes large differences in moments of $\mathcal{P}f_{\text{M}}$ between the theoretical values ($\int \text{d}^3vF(x)f_{\text{M}}$) and those evaluated by finite markers ($\int \text{d}^3vF(x)f_{\text{M}} \simeq \sum_k F(x_k)p_k$) where k is the index of a marker. In implementation, this difference results in bad convergence of the recursive method, in which the theoretical values are used to determine the factors (a, b, c). In the improved version, we do not use these theoretical values to make $\mathcal{P}f_{\text{M}}$, but the factors (a, b, c) are determined at every operation of collision term so that the conservation law is strictly satisfied. By

substituting Eqs. (6) and (7) in (4), we have

$$\sum_k \begin{pmatrix} F_k p_k & G_k \xi_k p_k & H_k p_k \\ F_k x_k^{1/2}\xi_k p_k & G_k x_k^{1/2}\xi_k^2 p_k & H_k x_k^{1/2}\xi_k p_k \\ F_k x_k p_k & G_k x_k \xi_k p_k & H_k x_k p_k \end{pmatrix}$$

$$\times \begin{pmatrix} a \\ b \\ c \end{pmatrix} = -\begin{pmatrix} \delta n \\ \delta P/v_{\text{th}} \\ \delta E/v_{\text{th}}^2 \end{pmatrix}, \qquad (8)$$

where abbreviations $F_k = F(x_k)$ and so on are used. In the limit of infinite number of markers, these factors should converge to their theoretical values.

As a test, a series of calculations with old and new field-particle operators were carried out. In Fig. 1, the residual relative errors in momentum and energy arising at an operation of $C_{\text{tp}} + \mathcal{P}f_{\text{M}}$ are compared between the old and new $\mathcal{P}f_{\text{M}}$ with varied marker numbers. In this test, the configuration space is neglected and only the collision operators in the velocity space are solved with initial δf given in the form of Eq. (5). Here, the relative residual error in momentum is evaluated as

$$\Delta P = \frac{\int \text{d}^3vv_{\parallel}[C_{\text{tp}}(\delta f) + \mathcal{P}f_{\text{M}}]}{\int \text{d}^3vv_{\parallel}\delta f},$$

and the residual error in energy ΔE is evaluated similarly. In the tests of old scheme, 3-time recursive operations of $\mathcal{P}f_{\text{M}}$ are used. In the old scheme, one can see that the numerical error is larger for the fewer-marker case. In the real simulation including configuration dependence and trapped particles, the error in the old operator is larger, and it is difficult to prepare enough markers to converge the error. On the other hand, the error in the new operator is just at the rounding-error level, even in the 1600-markers
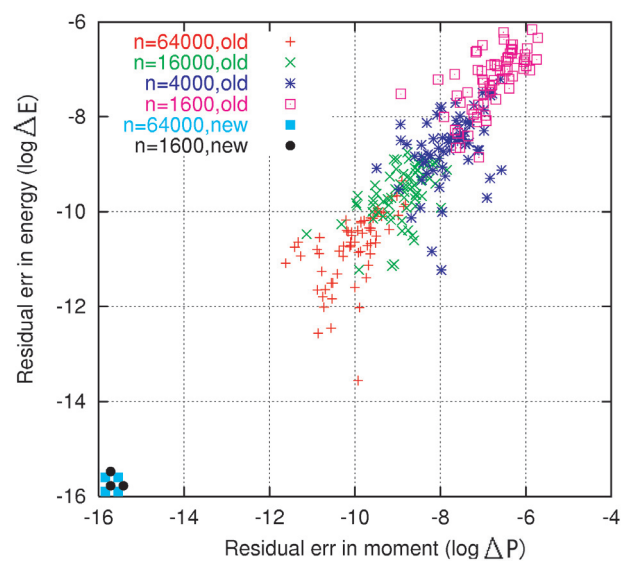

Fig. 1 Relative residual error in momentum and energy in one operation of $C_{\text{tp}} + \mathcal{P}f_{\text{M}}$. The time interval for the collision operation $\Delta t = 2 \times 10^{-3}\tau_{\text{ii}}$, and 200 samples are extracted for each test.

calculation. We have also confirmed the other property of the collision operator is also maintained in the new operator, i.e., the initial δf distribution given by Eq. (5) sustained its shape longer than the ion-ion collision time. Thus, the new field-particle operator shows better accuracy with less markers without changing its properties, which a proper linearized collision should hold, i.e., Eqs. (4) and (5). Although it is required to solve 3×3 matrices at every time step in the new scheme, the total computation time is shorter than that in the old recursive scheme.

4. Radial Meshes

The relation between neoclassical fluxes and radial electric field is solved on discrete meshes in the ρ-coordinate. Γ_i is evaluated using the volume averaged value between i-th and $(i + 1)$-th meshes as follows

$$\bar{\Gamma}_i(\rho_{i+\frac{1}{2}}) = \frac{1}{\Delta V_{i+1/2}} \int_{\Delta V_{i+1/2}} \mathrm{d}^3 x \int \mathrm{d}^3 v \dot{\rho} \delta f$$

$$= \frac{1}{\Delta V_{i+1/2}} \sum_{\{k | \rho_i \le \rho_k < \rho_{i+1}\}} w_k \dot{\rho}_k C(\rho_k, i), \qquad (9)$$

where the over-bar denotes an average value, k is the marker index, $\Delta V_{i+1/2}$ is volume enclosed by $\rho = \rho_i$ and ρ_{i+1} surfaces, and $C(\rho_k, i)$ is the shaping factor of a marker [21]. We have adopted a two-mesh wide triangle shaping factor to reduce spikes in Γ_i, which occurs when a large-weight marker goes across the grid. For electron flux, local value from the GSRAKE solution is referred to : $\Gamma_e(\rho_{i+1/2}) = \Gamma_e(\rho_{i+1/2}, E_\rho(\rho_{i+1/2}, t))$. Previously, the electric field was evaluated on the same point $\rho = \rho_{i+1/2}$ as Γ_i and Γ_e according to Eq. (2a). It is illustrated in the left hand side of Fig. 2. However, using this scheme, we found that the electric field profile attained an unphysical shape as shown in Fig. 3 with dashed blue line, where multiple roots for ambipolar condition are expected from GSRAKE solutions. Note that the radial electric field is converted using the relation $E_r[\mathrm{V}/m] = (1/a)E_\rho$ in Fig. 3. This is a test calculation using an LHD model configuration for the low-collisionality condition. The magnetic field strength at the magnetic axis is $B_0 = 1.65$ T, the major radius is $R_{\mathrm{ax}} = 3.7$ m, and the average minor radius is $a = 0.58$ m. The density, temperature, and rotational transform profiles are given as shown in Fig. 4. It is typical for LHD plasma to have multiple roots when T_e exceeds T_i. The GSRAKE solution both for Γ_i and Γ_e are used to estimate the ambipolar radial electric field that satisfies $\Gamma_i(\rho, E_\rho) = \Gamma_e(\rho, E_\rho)$, which is also plotted in Fig. 3. The E_ρ-profile obtained from the previous FORTEC-3D code neither connected ion-root to electron-root smoothly nor settled in a value guessed by GSRAKE. Mathematically, it is not an easy problem to obtain a continuous E_ρ-profile that satisfies the ambipolar condition $\Gamma_i = \Gamma_e$ point by point, if there are multiple roots for the ambipolar condition. A general way to solve this bifurcation problem is to introduce "electric field diffusivity" into Eq. (2a) as follows

$$\epsilon_0 \epsilon_\perp \frac{\partial E_\rho}{\partial t} = -e \left[z_i \Gamma_i - \Gamma_e \right] + \frac{1}{V'} \frac{\partial}{\partial \rho} \left(V' D_E \frac{\mathrm{d} E_\rho}{\mathrm{d}\rho} \right), \qquad (10)$$

where $V' = \mathrm{d}V/\mathrm{d}\rho$. The diffusion coefficient D_E either accounts for a higher-order correction to neoclassical transport due to the FOW effect in the presence of strong shear of the radial electric field around the transition layer from positive to negative root [22], or uses an empirical model of anomalous diffusion [23]. However, we do not employ this method in FORTEC-3D because of the following reasons: First, higher-order correction on ion neoclassical flux due to the FOW effect is already evaluated in Eq. (9) properly, since we trace the exact particle orbits in the presence of strong radial shear of E_ρ. Second, the FOW effect on electron neoclassical flux is negligible since the typical orbit width of electrons is $\sim \sqrt{m_e/m_i}$ times thinner than the ion one. Then GSRAKE solution based on a
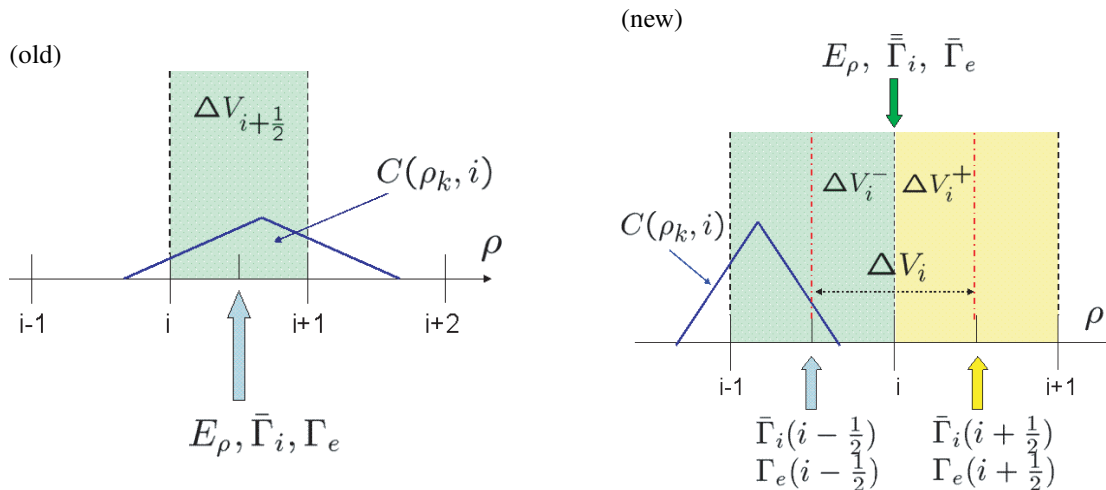

Fig. 2   Illustrations for radial meshes and positions on which fluxes and electric field are evaluated in old and new schemes.
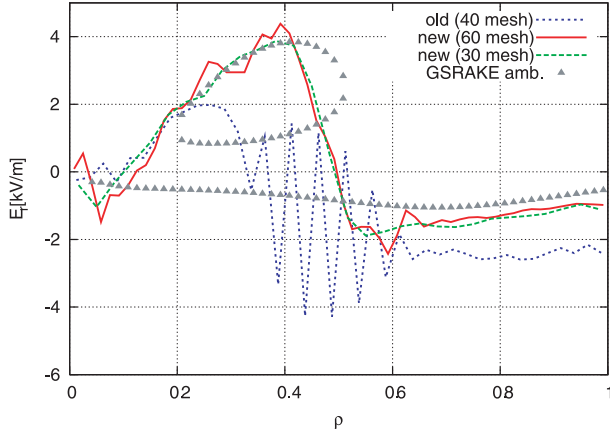
Fig. 3   Comparison of electric field profile between the old and new schemes for flux and electric field with different radial mesh numbers, at the time $t/\tau_i = 1.285$. Squares are estimations of ambipolar field from GSRAKE.
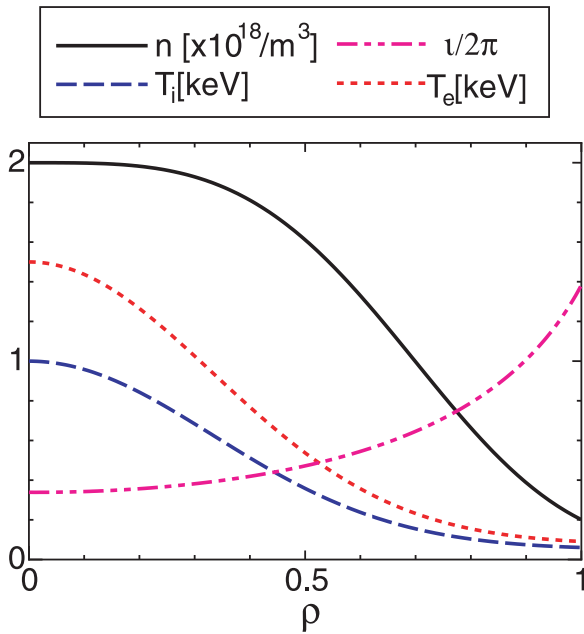

Fig. 4   Density, temperature, and rotational transform profiles obtained in the test simulations.

local transport theory is considered reasonable at least to explain electron transport even in the presence of strong E_ρ-shear at the transition layer. Third, it is known that the width of the transition layer connecting ion and electron roots is proportional to $\sqrt{D_E}$ and usually the anomalous electric diffusivity is assumed to be much larger than the neoclassical one [23]. Therefore, it is not proper to introduce such a parameter that controls the radial gradient scale into FORTEC-3D, with which we aim to study non-local effects in transport phenomena within the framework of the drift-kinetic equation.

Instead of introducing a diffusion term to avoid numerical difficulty in solving Eq. (2a), we solve this prob-

lem by improving the numerical method itself in FORTEC-3D. The unphysical bifurcation in previous calculations seems to have been caused by an improper numerical scheme to solve E_ρ-profile in the global simulation, where the time evolution of E_ρ was determined only by $\Gamma_{i,e}$ evaluated on the same mesh. Therefore, we adopted a new scheme that uses staggered-mesh for E_ρ and $\Gamma_{i,e}$, as illustrated in the right hand side of Fig. 2. Fluxes are evaluated on half-grids $\rho = \rho_{i\pm1/2}$ and time evolution of $E_\rho(\rho_i)$ is calculated on the full-grids as follows

$$\epsilon_0 \epsilon_\perp \frac{\partial E_\rho(\rho_i)}{\partial t} = -e\left[z_i \bar{\bar{\Gamma}}_i(\rho_i) - \bar{\Gamma}_e(\rho_i)\right],\qquad (11)$$

where $\bar{\bar{\Gamma}}_i(\rho_i)$ and $\bar{\Gamma}_e(\rho_i)$ are averaged values of those evaluated at $\rho = \rho_{i\pm1/2}$ determined in the following way. First, note that the volume-averaged flux around $\rho = \rho_i$ grid is given by

$$\bar{\Gamma}(\rho_i) = \frac{1}{\Delta V_i} \int_{\rho_{i-\frac{1}{2}}}^{\rho_{i+\frac{1}{2}}} d\rho \, V'\Gamma(\rho) = \frac{1}{\Delta V_i} \int_{V(\rho_{i-1/2})}^{V(\rho_{i+1/2})} dV \, \Gamma(V),$$
$$(12)$$

where the subscript i or e for particle species is omitted here. In computation, we do not know the true value of the flux $\Gamma(V)$, but by expanding $\Gamma(V)$ around $V_i = V(\rho_i)$, one finds that the accuracy of the above expression is

$$\bar{\Gamma}(V_i) = \Gamma(V_i) + \frac{\Delta V_i^{+2} - \Delta V_i^{-2}}{2\Delta V_i} \frac{d\Gamma}{dV}\Big|_{V_i} + \cdots$$
$$= \Gamma(V_i) + \frac{\Delta V_i^+ - \Delta V_i^-}{2} \frac{d\Gamma}{dV}\Big|_{V_i} + \cdots$$
$$= \Gamma(V_i)\left[1 + O\left(\frac{\Delta\rho^2 V''}{\Gamma} \frac{d\Gamma}{dV}\right)\right],\qquad (13)$$

where $\Delta V_i^\pm = \pm(V_{i\pm1/2} - V_i)$, $\Delta V_i^+ + \Delta V_i^- = \Delta V_i$ and order estimation $\Delta V_i^+ - \Delta V_i^- \sim \Delta\rho^2 V_i''$ is used. Note here that $\Delta V_i^+ - \Delta V_i^- \neq 0$, since we take uniform mesh not in V, but in ρ. Next, for the staggered-mesh scheme, we consider a linear interpolation of $\Gamma(V_i)$ as a function of V as follows

$$\Gamma(V_i) = \frac{1}{\Delta V_i}\left[\Delta V_i^+ \Gamma(V_{i-1/2}) + \Delta V_i^- \Gamma(V_{i+1/2})\right]$$
$$\times \left[1 + O\left(\frac{\Delta V^2}{\Gamma} \frac{d^2\Gamma}{dV^2}\right)\right],\qquad (14)$$

In order to introduce a smoothing effect in evaluating flux, however, we do not simply replace $\Gamma(V_{i\pm1/2})$ in Eq. (14) with $\bar{\Gamma}(\rho_{i\pm1/2})$ but assume that the ion flux $\Gamma_i(\rho_i)$ can be approximated by $\bar{\bar{\Gamma}}_i(\rho_i)$ defined as follows

$$\bar{\bar{\Gamma}}_i(\rho_i) = \left[W_{i-}\bar{\Gamma}_i(\rho_{i-1/2}) + W_{i+}\bar{\Gamma}_i(\rho_{i+1/2})\right],\qquad (15)$$

with these two constraints to determine the weight factors $W_{i\pm}$,

$$W_{i+} + W_{i-} = 1.\qquad (16a)$$

If $V'_{i-1/2}\bar{\Gamma}(\rho_{i-1/2}) = V'_{i+1/2}\bar{\Gamma}(\rho_{i+1/2}) = C$,

then $V'_i \bar{\bar{\Gamma}}(\rho_i) = C.\qquad (16b)$

Note that the double-over-bar means that $\bar{\bar{\Gamma}}(\rho_i)$ is an average value of the volume-average values $\bar{\Gamma}(\rho_{i\pm1/2})$. The first constraint means that this average is a linear interpolation similar to Eq. (14), and the second constraint comes from the consideration that $V'\Gamma(\rho)$ is the total particle number passing across the ρ = const. surface in unit time. The latter is a continuity condition for flux, which serves to avoid virtual accumulation or diffusion of particles in the volume ΔV_i when the particle flux passing through both sides of the volume are balanced. Equation (16) can be solved for $W_{i\pm}$ and we have

$$W_{i+} = \frac{V'_{i+1/2}}{V'_i} \cdot \frac{(V'_i - V'_{i-1/2})}{(V'_{i+1/2} - V'_{i-1/2})}, \tag{17a}$$

$$W_{i-} = \frac{V'_{i-1/2}}{V'_i} \cdot \frac{(V'_{i+1/2} - V'_i)}{(V'_{i+1/2} - V'_{i-1/2})}. \tag{17b}$$

While $\bar{\bar{\Gamma}}_i(\rho_i)$ is evaluated from non-local information in the range $\rho_{i-1} \leq \rho \leq \rho_{i+1}$, the width of the shaping factor is shrunk half than in the previous scheme in order to avoid too much non-locality being included in the evaluation of $\bar{\bar{\Gamma}}_i(\rho_i)$, as illustrated in the right hand side of Fig. 2. It is found that the ratio of the weights are close to that appearing in Eq. (14), that is, $W_{i-} : W_{i+} \simeq \Delta V_i^+ : \Delta V_i^-$. The proof is shown in the Appendix. Therefore, Eq. (15) properly provides a linear interpolation of Γ at $V = V(\rho_i)$ from $\bar{\Gamma}(V(\rho_{i-1/2}))$ and $\bar{\Gamma}(V(\rho_{i+1/2}))$ with an additional constraint Eq. (16b) for numerical stability. Moreover, since $W_{i-} \simeq W_{i+} \simeq 1/2$ and Eq. (15) can be rewritten as

$$\bar{\bar{\Gamma}}(\rho_i) \simeq \bar{\Gamma}(\rho_i) + \frac{1}{2}\left[\bar{\Gamma}(\rho_{i+1/2}) + \bar{\Gamma}(\rho_{i-1/2}) - 2\bar{\Gamma}(\rho_i)\right]$$

$$\simeq \bar{\Gamma}(\rho_i) + \frac{\Delta\rho^2}{2}\frac{d^2\bar{\Gamma}(\rho_i)}{d\rho^2},$$

the evaluation of fluxes according to Eq. (15) brings a numerical diffusion to $\bar{\bar{\Gamma}}$, which is also thought to stabilize the time evolution of radial electric field. For electrons, average value $\bar{\Gamma}_e(\rho_i)$ is evaluated in the same way as for ions from GSRAKE solutions at $\rho = \rho_{i\pm1/2}$ as follows

$$\bar{\Gamma}_e(\rho_i) = \Big[W_{i-}\Gamma_e(\rho_{i-1/2}, E_\rho(\rho_{i-1/2}))$$

$$+ W_{i+}\Gamma_e(\rho_{i+1/2}, E_\rho(\rho_{i+1/2}))\Big], \tag{18}$$

where Γ_e-s on the right side are not the volume-average values $\bar{\Gamma}_e$ since GSRAKE solutions are given as local values based on the local transport theory.

With this new scheme, FORTEC-3D can simulate continuous transition both in time and space from ion- to electron-root as shown in Fig. 3 with red and green lines. The same configuration as in the old simulation was used. It is to be noted that the number of radial meshes in the new simulations is 60 (red) or 30 (green), while it was 40 (blue) for the old simulation. However, we had already attempted a 80-mesh calculation with old scheme, which have resulted in a similar unphysical E_ρ-profile. Therefore, it is not because the radial resolution was not sufficient to express the transition layer of E_ρ that the previous FORTEC-3D failed in solving bifurcated state of radial

electric field. In contrast, using the new scheme, the E_ρ-profile shows a smooth and continuous transition between ion and electron roots, and the width of the transition layer is not affected by the radial mesh size. The transition layer width in Fig. 2 is about 0.15, and the mesh size $\Delta\rho = 1/30$ or $1/60$ is then sufficiently small to mask the effect of numerical diffusion in the formation and propagation of the layer. As it is shown in the Appendix, the new scheme has the same accuracy as the previous one, judging from the order estimation. In the new scheme, however, existence of the radial gradient $\Gamma(\rho)$ is taken into consideration to evaluate $\bar{\bar{\Gamma}}$ based on the linear interpolation Eq. (14) with a subsidiary condition Eq. (16b) for numerical stability, and it is considered that the staggered-meshes to evaluate the average flux and time evolution of the electric field, along with the numerical diffusion effect within, serves to obtain smooth transition in the simulation. Note that the radial electric field profile of the new scheme was obtained at a moment when it was transiting from negative to positive root. The time evolution of the electric field profile toward a quasi-steady state is shown in the next section.

5. Filtration

Reducing the numerical noise without relying on a massive number of markers is essential to any Monte-Carlo simulation. In the δf method, the origin of big noise is from markers that have huge weights w or p. Let us reconsider the equation of particle weights Eq. (3) to understand the origin of huge-weight markers. If collisions are neglected, Eq. (3b) can be rewritten as follows

$$\frac{d\ln p}{dt} = \frac{d\rho}{dt}\frac{\partial}{\partial\rho}\ln f_M(\rho, \mathcal{K}) + \frac{d\mathcal{K}}{dt}\frac{\partial}{\partial\mathcal{K}}\ln f_M(\rho, \mathcal{K}),$$

$$\Leftrightarrow d\ln p = d\ln f_M(\rho, \mathcal{K}), \tag{19}$$

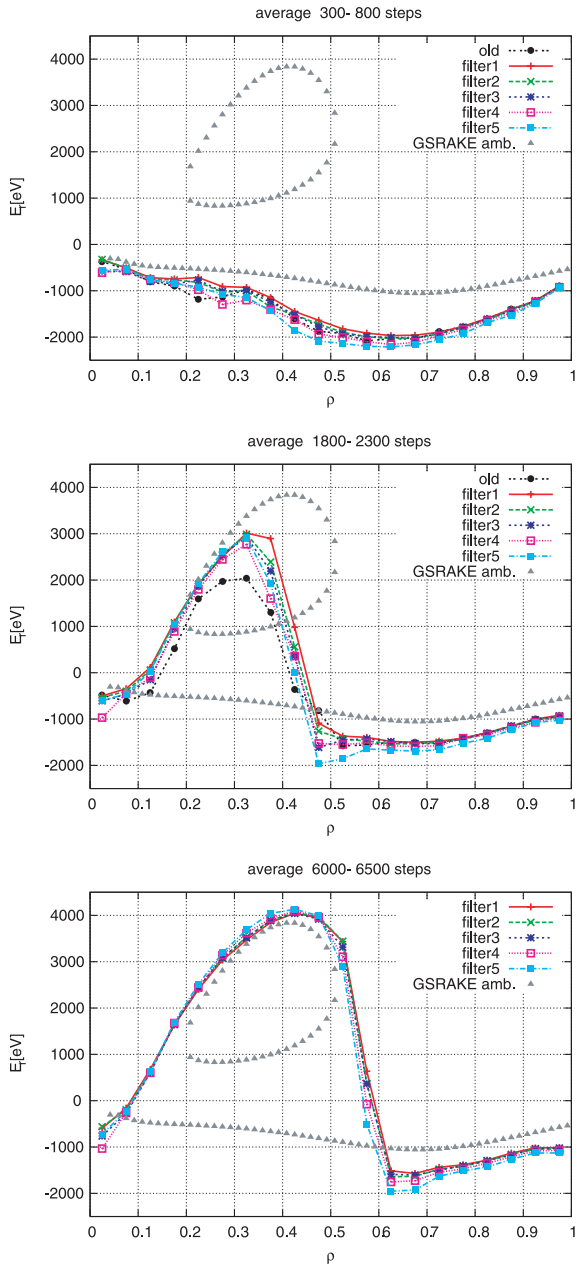where $d\rho/dt = \boldsymbol{v}_d \cdot \nabla\rho$. Then the marker weights can be determined as

$$p_1 = p_0\frac{n_1}{n_0}\left(\frac{T_0}{T_1}\right)^{3/2}\exp\left[-\frac{\mathcal{K}_1}{T_1} + \frac{\mathcal{K}_0}{T_0}\right], \tag{20a}$$

$$w_1 = w_0 - (p_1 - p_0), \tag{20b}$$

where subscript 0 and 1 represents the values of them on marker's position at the time $t = t_0$ and t_1. In practice, the change of weights by marker's guiding-center motion is determined using the relation above, since it does not need to evaluate any derivatives numerically. Moreover, it is a positivity-preserving scheme for p if the initial value p_0 is positive. From Eqs. (20), it is realized that markers that travel long distance in radial directions will have large marker weights since n and T always have gradient in the ρ-direction. In contrast to axisymmetric tokamaks, in which time-average radial position of a particle do not drift in the collisionless limit, it is inevitable to have such large-drift particles in helical plasmas, especially in low-collisionality cases. Therefore we need to set limits for weight values. In reality, we found that only

Table 1 Filter strengths and marker numbers used in test simulations.

	p	$|w|/p$	v/v_{th}	marker num.
old	-	2.0	5.0	3.84×10^7
filter 1	5	2.0	4.5	3.84×10^7
filter 2	8	2.5	4.5	3.84×10^7
filter 3	10	2.5	4.5	1.28×10^7
filter 4	25	4.0	4.5	1.92×10^7
filter 5	10	10.0	4.5	1.92×10^7

Fig. 5 Comparison of electric field profiles between old and new schemes for different filters at three periods. Plotting points are reduced to 20 here, although E_r is evaluated at 60 points in the simulations.
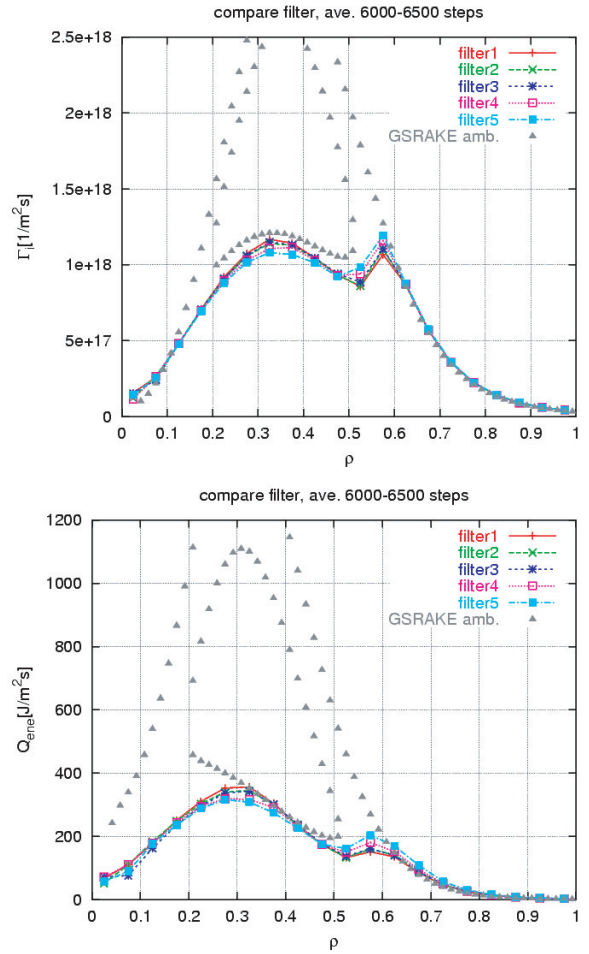

Fig. 6 Comparison of radial profile of the radial ion particle and energy fluxes among different filters at time steps between 6000 to 6500, when the radial electric field almost reaches the quasi-steady state.

less than 0.1% of simulation markers have huge weights $p_1 \sim |w_1| \gg 10^2 \sim 10^3 p_0$, and these markers make the

calculation very noisy and unstable. To exclude the noise, we apply filters for marker weights by setting limits for $|w|/p$, v/v_{th}, and p. The first limiter follows from the assumption in the δf method that $|\delta f|/f_{\mathrm{M}} \ll 1$, and the second limiter is adopted because fast ions tend to have large orbit widths and drift velocity. The third one was introduced after we have found that the huge-$|w|$ markers could not be eliminated effectively only by the first filter, but from Eq. (20b) it is expected that large $|w|$ coincides with large p. The markers breaking these limits are filtrated out and recycled around the magnetic axis, which contributes to maintain marker population there. This method is an extension of the marker recycling technique at the outermost surface $\rho = 1$, which already has been equipped with previous FORTEC-3D. The details of recycling and determining new weights for those recycled markers are explained in Ref. [9].

To check the effect of filters, we have conducted several tests with varied strength of filters as shown in Table 1. The same configuration as used in Sec. 4 is used. Note here that the "old" simulation used the old $\mathcal{P}$ operator and the

new flux-evaluation scheme, but was not equipped with filters for the weight p. In Fig. 5, comparisons of radial electric field at three different times with varied filters are shown. Note that the simulation of the old scheme stopped around 3800 steps because of huge noise. As shown there, the time evolution of E_ρ and quasi-steady state profiles (the last figure of the three) are almost the same regardless of the strength of filters. In addition, the transition from ion- to electron-root propagates at almost the same pace among these simulations. Profiles of the ion particle flux Γ_i and energy flux $Q_{ene} = \langle \int d^3 v \dot{\rho} \mathcal{K} \delta f / |\nabla \rho| \rangle$ at the quasi-steady state are also compared among different filters in Fig. 6. It is confirmed that the strength of the filters does not affect the neoclassical transport level so much, at most 10% for Γ_i and 20% for Q_{ene} between the results with filter-1 and filter-5. We can also see that the neoclassical fluxes Γ_i and Q_{ene} obtained from FORTEC-3D agree with the GSRAKE solutions. The fluxes are reduced to the electron-root level at $0.2 < \rho < 0.5$, which is a good example of the improvement scenario of plasma confinement by positive-E_ρ in LHD plasmas.

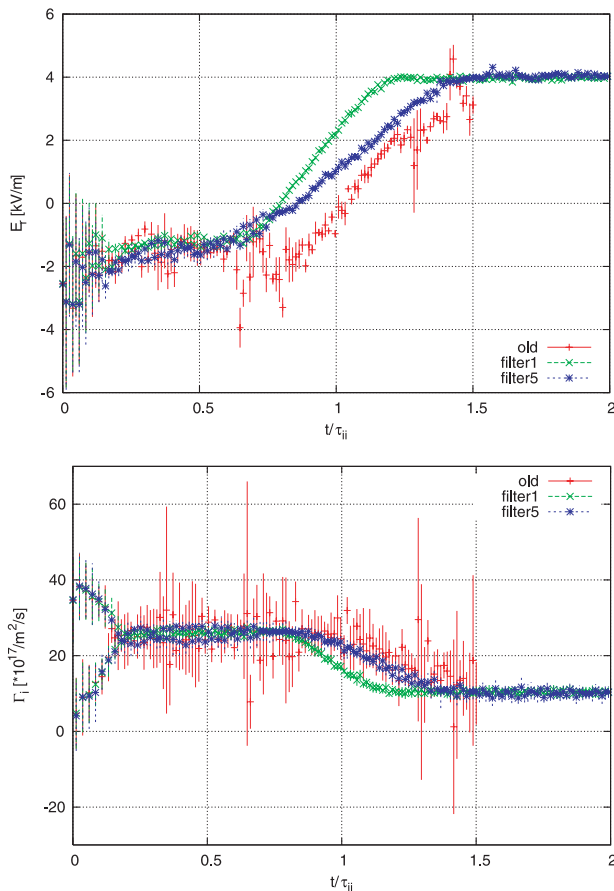To examine the time evolution in detail, we compare E_ρ and Γ_i on $\rho = 0.45$ surface for three different filters in Fig. 7. Here, error-bars are evaluated from the variance between every 30 steps. It is found that the filters successfully suppress the numerical noise even by the weakest filter, although the start timing of transition differs slightly among three simulations. Therefore the 10% difference in neoclassical flux between filter-1 and filter-5 can be attributed to the fact the filter-1 is too strong. To reduce the numerical noise without affecting observable values such as Γ_i and Q_{ene}, a very weak filter is found to be both preferable and sufficient. It is also notable that the simulation marker number can be reduced without increasing the noise level, if we adopt the filters.

In Fig. 8, the marker distributions of which are filtrated out are plotted in the (θ, ζ)-space and the $(v_\parallel, v_\perp)$-space for the filter-3 case. Note that the distribution of

Fig. 7 Comparison of time evolution of E_r and Γ_i among old, filter-1, and filter-5 calculations on $\rho = 0.45$ surface. The oscillation at the beginning phase is GAM. Time is normalized by the ion collision time $\tau_i (\rho = 0.5) \simeq 2.66$ ms, and $1\tau_i$ corresponds to 2500 steps in the simulation.
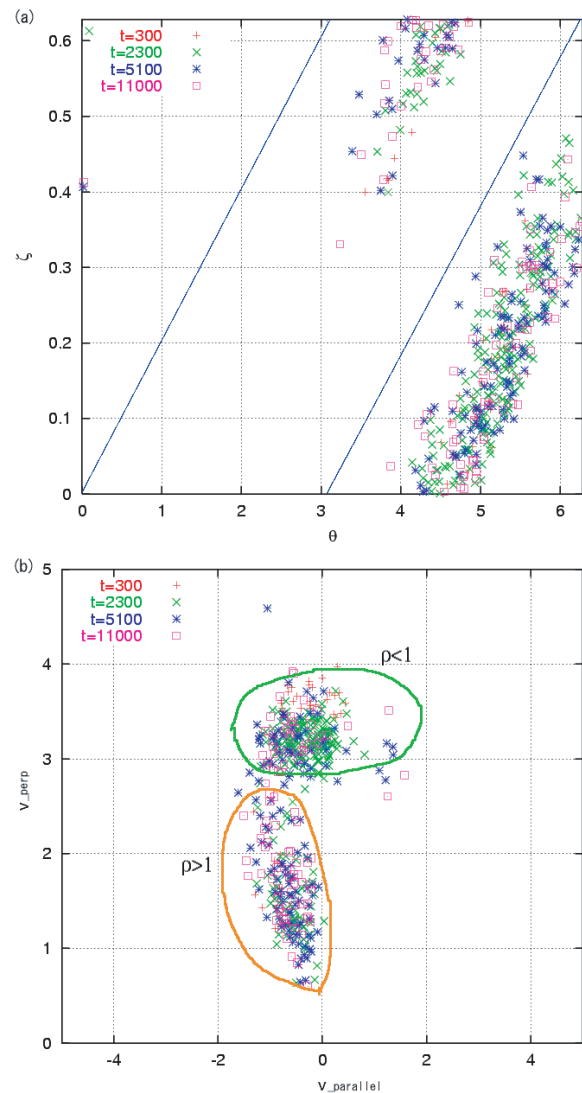

Fig. 8 Filtrated marker distribution in (a): (θ, ζ)-space and (b): $(v_\parallel, v_\perp)$-space, for the filter-3 case at four different moments. The blue lines in Fig. 8 (a) show the position of helical coils. In Fig. 8 (b), the radial positions where markers are eliminated are also indicated.
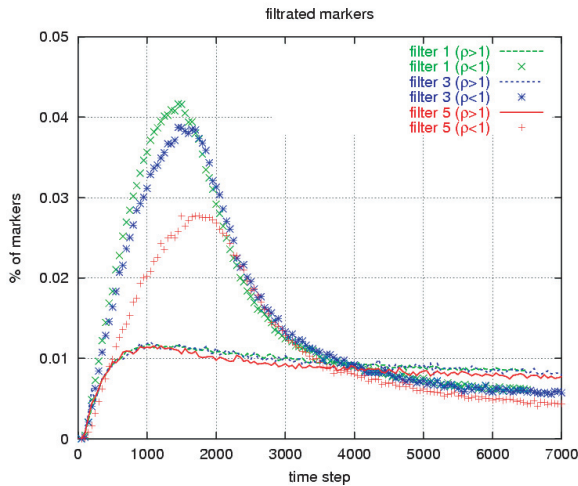
Fig. 9 Comparison of the % of markers filtrated among the simulation filter-1, 3, and 5. The symbols represents the number of markers that break the limit for the weights and velocity, while the lines represent those who escape from the $\rho = 1$ surface.
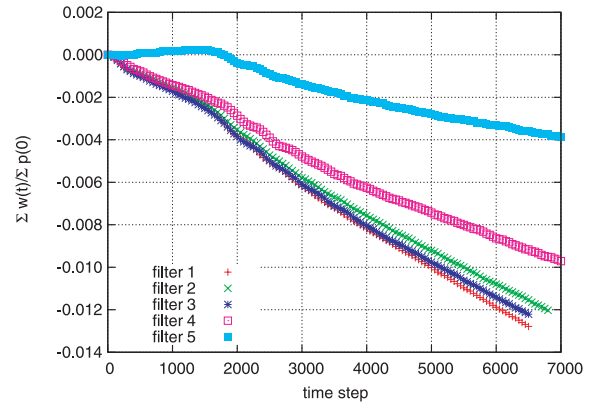

Fig. 10 Comparison of the time evolution of the value $\sum_k w_k(t) / \sum_k p_k(t = 0)$ among filter-1 to -5. The sums are taken over the whole markers inside the plasma, $\rho < 1$.

the markers that escaped from the outermost surface are also plotted in those figures. It can be seen that the filtrated markers range in $|v_\parallel|/v_\perp \ll 1$, $v/v_{\rm th} > 3$ and between the helical coils, which shows that the markers with huge weights are indeed deeply trapped, high-speed particles as expected. As mentioned in Ref. [16], putting filters on marker weights corresponds to the δf simulations in which DKE is solved only in a thin layer around a flux-surface and remove markers that escape from the thin layer [15, 24]. Then it should be carefully verified how much the filtering scheme screens the non-local effects on neoclassical transport from large-orbit particles, which we intend to study with the FORTEC-3D global transport simulation. Concerning the test calculations shown here, the filter strength is very weak compared with that used in Ref. [16] where the filter $|\delta f|/f_{\rm M}(\sim |w|/p) < 0.01$ was applied. As a result, the fraction of markers that are filtrated in our simulation is less than 0.05% at most, as shown in Fig. 9. The effect of the filters on the conservation of particle numbers is also checked. In Fig. 10, the time change of the value

$$\frac{\int {\rm d}^3 x \int {\rm d}^3 v \delta f(X, v, t)}{\int {\rm d}^3 x \int {\rm d}^3 v f_M(X, v)} \simeq \frac{\sum_k w_k(t)}{\sum_k p_k(t = 0)}$$

in each simulation is plotted, where the volume integral is evaluated in the whole plasma volume. As the simulation system has an open boundary at $\rho = 1$, there is no strict conservation of the total particle number, momentum, and energy. However, the strength of the filters do affect the change in the total particle number. As expected, the conservation of particle number is better for weaker filters. One can also see in Fig. 10 that the requirement $|\delta f|/f_{\rm M} \ll 1$ is well satisfied in the sense of volume-average with the weakest filter, filter-5, while this filter al-

lows a marker has $|w|/p \sim 10$, that is, $|\delta f|/f_{\rm M}$ could be much larger than unity on some local points in the phase space. Although the δf formulation assumes $|\delta f|/f_{\rm M} \ll 1$, this assumption is actually used only to neglect the non-linear collision term $C(\delta f, \delta f)$ to derive the DKE, Eq. (1), and we expect that only a weak filter for weight and velocity is sufficient to reduce statistical noise but retain conservation property and the FOW effects on transport. More detailed study will be done as FORTEC-3D is applied to non-local transport study.

6. Discussion and Conclusion

The improvements for numerical schemes in FORTEC-3D were proved to reduce numerical errors and noises significantly with tolerable changes in the observable values such as flux and electric field. FORTEC-3D will be applied to study the FOW effects in helical plasmas, transition phenomena of radial electric field, and so on.

We have discussed the FOW effect on the ion-root E_ρ profile in Ref. [9]. It has been found that the ion-root E_ρ usually becomes more negatively large in FORTEC-3D simulations compared with the GSRAKE estimation, as one can also see in Fig. 5 at $\rho > 0.6$. On the other hand, $\Gamma_{\rm i}$ and $Q_{\rm ene}$ show little difference with the GSRAKE solutions in the present simulations. Remarkable difference can only be seen in the $Q_{\rm ene}$ profile near the magnetic axis $\rho < 0.2$, where the energy flux is strongly suppressed. Since this region corresponds to the inner transition layer, the existence of the sheared E_ρ profile requires non-local treatment in neoclassical transport analysis. It is also anticipated that large-orbit-width particles like potato particles [5, 6] in tokamak core would appear in the region near the axis of LHD, and reduce the energy transport there [14, 25]. However, since the model profile used here has a transition layer close to the magnetic axis, it is difficult to study separately these two possible factors, which will include the FOW effect in the core neoclassi-

cal transport. This problem will be studied using a simpler model profile near the future. We are also planning to apply the δf method to solve electron transport and evaluate the bootstrap current in the presence of ambipolar electric field.

Acknowledgment

Appendix. Proof for $W_{i-} : W_{i+} \simeq \Delta V_i^+ : \Delta V_i^-$

First, consider that $W_{i\pm}^0$ are taken so that they exactly satisfy the relations

$$W_{i-}^0 : W_{i+}^0 = \Delta V_i^+ : \Delta V_i^-, \tag{A.1}$$

$$W_{i-}^0 + W_{i+}^0 = 1. \tag{A.2}$$

Next, the difference between W_{i+} and W_{i+}^0 is described as ϵ, that is,

$$W_{i+} = W_{i+}^0 + \epsilon, \quad W_{i-} = W_{i-}^0 - \epsilon. \tag{A.3}$$

Using the relations in Eqs. (A.1) and (A.2), it follows

$$\frac{W_{i+}\Delta V_i^+ - W_{i-}\Delta V_i^-}{\Delta V_i} = \epsilon. \tag{A.4}$$

Substituting Eq. (17) into Eq. (A.4) and using the approximations $V_i' \simeq (V_{i+1/2}' + V_{i-1/2}')/2$, $\Delta V_i \simeq \Delta\rho(V_{i+1/2}' + V_{i-1/2}')$ and $\Delta V_i^\pm \simeq \Delta\rho(V_i' + V_{i\pm1/2}')/2$, we have

$$\epsilon \simeq \frac{3(V_{i+1/2}' - V_{i-1/2}')}{4(V_{i+1/2}' + V_{i-1/2}')} \sim O\left(\frac{\Delta\rho V_i''}{V_i'}\right) \sim O\left(\frac{\Delta S}{S}\right), \tag{A.5}$$

where S is the surface cross-section of $\rho = \rho_i$ flux-surface and $\Delta S \sim S(\rho_{i+1/2}) - S(\rho_{i-1/2})$. Therefore, as far as sufficiently small radial mesh size is used, we can regard $\epsilon \ll 1$. For example, in the case of LHD model configuration we used here, $|\epsilon| < 0.03$ for 60 radial meshes.

The effect of the error ϵ to the interpolation of flux can also be evaluated. By substituting Eq. (A.3) into Eq. (15), one obtains

$$\begin{aligned}
\bar{\bar{\Gamma}}(\rho_i) &= W_{i-}^0 \bar{\Gamma}(\rho_{i-1/2}) + W_{i+}^0 \bar{\Gamma}(\rho_{i+1/2}) \\
&\quad + \epsilon\left(\bar{\Gamma}(\rho_{i+1/2}) - \bar{\Gamma}(\rho_{i-1/2})\right) \\
&= \frac{1}{\Delta V_i}\left[\Delta V_i^+ \bar{\Gamma}(\rho_{i-1/2}) + \Delta V_i^- \bar{\Gamma}(\rho_{i+1/2})\right] \\
&\quad \times \left[1 + O\left(\frac{\Delta\rho^2 V''}{\Gamma}\frac{d\Gamma}{dV}\right)\right].
\end{aligned} \tag{A.6}$$

Thus $\bar{\bar{\Gamma}}$ has at least the same order of accuracy as $\bar{\Gamma}$.

[1] D.E. Hastings *et al.*, Nucl. Fusion **25**, 445 (1985).
[2] R. Kanno *et al.*, Nucl. Fusion **37**, 1463 (1997).
[3] N. Nakajima *et al.*, J. Phys. Soc. Japan **61**, 833 (1992).
[4] M. Wakatani, *Stellarators and Heliotron Devices* (Oxford Univ. Press, 1998), Chap. 7.
[5] P. Helander, Phys. Plasmas **7**, 2878 (2000).
[6] S. Satake *et al.*, Phys. Plasmas **9**, 3946 (2002) .
[7] K. Nagaoka *et al.*, *"Ion Heating Experiments Using Perpendicular Neutral Beam Injection in the Large Helical Device,"* Proceedings of Joint Conf. ITC17 and ISHW16, O-11 (2007).
[8] N. Winsor *et al.*, Phys. Fluids **11**, 2448 (1968).
[9] S. Satake *et al.*, Plasma Fusion Res. **1**, 002 (2006).
[10] S. Satake *et al.*, Nucl. Fusion **45**, 1362 (2005).
[11] S. Satake *et al.*, Nucl. Fusion **47**, 1258 (2007).
[12] W.X. Wang *et al.*, Plasma Phys. Control. Fusion **41**, 1091 (1999).
[13] S. Brunner *et al.*, Phys. Plasmas **6**, 4504 (1999).
[14] W.X. Wang *et al.*, Phys. Plasmas **13**, 082501 (2006).
[15] J.L. Lewandowski *et al.*, Phys. Plasmas **8**, 2849 (2001).
[16] M. Yu. Isaev *et al.*, Fusion Sci. Technol. **50**, 440 (2006).
[17] C.D. Beidler *et al.*, Plasma Phys. Control. Fusion **43**, 1131 (2001).
[18] S.P. Hirshman *et al.*, J. Comput. Phys. **96**, 99 (1991).
[19] A.H. Boozer, Phys. Fluids **23**, 904 (1980).
[20] Z. Lin *et al.*, Phys. Plasmas **2**, 2975 (1995).
[21] C.K. Birdsall *et al.*, *Plasma Physics via Computer Simulation* (Inst. Phys. Pub., 1991), Chap. 4.
[22] D.E. Hastings Phys. Fluids **28**, 334 (1985).
[23] S. Toda and K. Itoh, Plasma Phys. Control. Fusion **46**, 1039 (2004).
[24] M. Sasinowski and A.H. Boozer, Phys. Plasmas **2**, 610 (1995).
[25] A. Bergmann *et al.*, Phys. Plasmas **12**, 5192 (2001).